

Inversion of the attenuated V-line transform for SPECT with Compton cameras

Markus Haltmeier[†] Sunghwan Moon[‡] Daniela Schiefeneder[†]

[†]Department of Mathematics, University of Innsbruck
Technikerstrasse 13, A-6020 Innsbruck, Austria
{Daniela.Schiefeneder, Markus.Haltmeier}@uibk.ac.at

[‡]Department of Mathematical Sciences, Ulsan National Institute of Science and Technology
Ulsan 44919, Republic of Korea.
shmoon@unist.ac.kr

Abstract

The Compton camera is a promising alternative to the Anger camera for imaging gamma radiation, with the potential to significantly increase the sensitivity of SPECT. Two-dimensional Compton camera image reconstruction can be implemented by inversion of the V-line transform, which integrates the emission distribution over V-lines (unions of two half-lines), that have vertices on a surrounding detector array. Inversion of the V-line transform without attenuation has recently been addressed by several authors. However, it is well known from standard SPECT that ignoring attenuation can significantly degrade the quality of the reconstructed image. In this paper we address this issue and study the attenuated V-line transform accounting for attenuation of photons in SPECT with Compton cameras. We derive an analytic inversion approach based on circular harmonics expansion, and show uniqueness of reconstruction for the attenuated V-line transform. We further develop a discrete image reconstruction algorithm based on our analytic studies, and present numerical results that demonstrate the effectiveness of our algorithm.

Keywords: Compton cameras, SPECT, attenuation correction, V-line transform, Radon transform, image reconstruction.

1 Introduction

Single photon emission computed tomography (SPECT) is a major medical diagnosis tool for functional imaging. Current SPECT systems are based on the Anger camera for gamma ray detection [5], which uses collimators and typically records only one out of 10 000 actually emitted photons. This yields to a large noise level despite long recording times, and consequently results in poor spatial and temporal resolution. In order to increase the number of recorded photons, the concept of Compton cameras has been developed in [13, 33, 38].

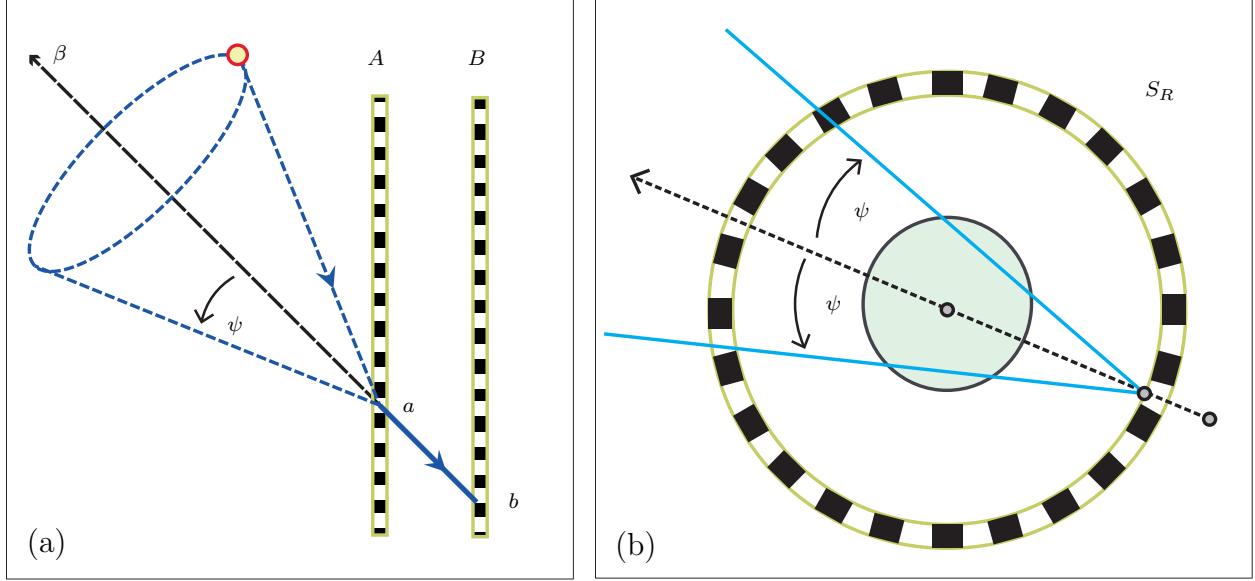


Figure 1.1: (a) Compton camera consists of two detector arrays and any observed photon can be traced back to the surface of a cone. (b) One-dimensional circular Compton camera. The conical integrals reduce to integrals over V-shaped, with the vertex on S_R and the symmetry axis pointing to the origin.

The data in SPECT with Compton cameras consist of averages of the marker distribution over conical surfaces or V-shaped lines. Several authors studied analytical approaches for image reconstruction from Compton camera data [1, 7, 8, 11, 14, 16, 19, 20, 22, 24–27, 32, 34–36]. However, in all these works the effect of the attenuation of photon has been neglected. As in the case of standard SPECT, this can result in significant degradation of image quality. In this work we establish a analytic reconstruction approach for Compton camera imaging accounting for attenuation, which, to the best of our knowledge, is the first in such a direction.

1.1 SPECT with Compton cameras

In SPECT, weakly radioactive tracers are given to a patient and are detected through the emission of gamma ray photons. Standard devices for photon detection in SPECT use Anger cameras based on collimation. These kind of detectors only record photons that enter the detector vertically and therefore remove most photons. Compton cameras do not require a collimator and in principle are capable of recording all photons that are emitted in the direction of the detector array [13, 33, 38]. Such devices consist of a scatter detector array A and an absorption detector array B . As shown in Fig. 1.1(a), a gamma ray photon arriving at the Compton camera undergoes Compton scattering in A and is absorbed in B . Both detector arrays are position and energy sensitive, and the measured energies can be used to determine the scattering angle via the Compton scattering formula. One concludes that the detected photon must have been emitted on the surface of a circular cone. Consequently, for a distribution of tracers, the Compton camera approximately provides integrals of the marker distribution over conical surfaces.

In this paper we consider two-dimensional Compton camera imaging, where the conical surfaces reduce to V-lines with vertices on a circle; see Fig. 1.1(b). This two-dimensional version arises for one-dimensional Compton camera proposed in [6] when the marker distribution is either supported in a plane or the detectors are collimated to this plane.

1.2 The attenuated V-line transform

We denote by $D_R := \{x \in \mathbb{R}^2 \mid \|x\| < R\}$ the unit disc in \mathbb{R}^2 and by S_R the surrounding circle. $C_c^\infty(D_R)$ denotes the set of all smooth functions $f: \mathbb{R}^2 \rightarrow \mathbb{R}$ with $\text{supp}(f) \subseteq D_R$. For any angle $\varphi \in \mathbb{R}$ we write $\Phi(\varphi) := (\cos \varphi, \sin \varphi)$ and $\Phi(\varphi)^\perp := (-\sin \varphi, \cos \varphi)$ such that $(\Phi(\varphi), \Phi(\varphi)^\perp)$ forms a positive oriented orthonormal basis of \mathbb{R}^2 . Further we denote by $\mu \in \mathbb{R}$ any attenuation value. In practice we have $\mu \geq 0$. However since most of the following holds for general μ , we make restrictions on μ only when necessary.

Definition 1.1. The attenuated V-line transform $\mathcal{V}_\mu f: [0, 2\pi) \times (0, \pi/2) \rightarrow \mathbb{R}$ (with attenuation parameter μ) of $f \in C_c^\infty(D_R)$ is defined by

$$\mathcal{V}_\mu f(\varphi, \psi) := \sum_{\sigma=\pm 1} \int_0^\infty f(R\Phi(\varphi) - r\Phi(\varphi - \sigma\psi)) e^{-\mu r} dr. \quad (1.1)$$

The attenuated V-line transform consists of integrals of the emitter distribution over V-lines (the union of two half-lines) having the vertex $R\Phi(\varphi)$, symmetry axis $\{-r\Phi(\varphi) \mid r > 0\}$ and half opening angle ψ . The factor $e^{-\mu r}$ accounts for the attenuation of photons when propagating a distance r in homogeneous media with attenuation value μ . In our numerical simulation studies we use $\mu = 0.15$ /cm, which is a realistic value for soft tissue.

1.3 Outline of main results

In this paper we study the problem of reconstructing the emitter distribution f from $\mathcal{V}_\mu f$. Our main contributions can be summarized as follows.

- ① **FOURIER SERIES DECOMPOSITION:** Let f_n and g_n denote the Fourier coefficients with respect to the polar angle of f and the vertex position of $\mathcal{V}_\mu f$, respectively. In Section 2, we derive an integral equation for f_n in terms of g_n with an explicitly given kernel of the generalized Abel type (see Eq. (2.10)).
- ② **UNIQUENESS OF RECONSTRUCTION:** In Section 3 we show that the generalized Abel equation (2.10) has a unique solution and therefore f_n can be uniquely recovered from g_n by solving (2.10); see Thm. 3.2. In particular, this implies uniqueness of reconstruction of the attenuated V-line transform in the sense that any data $\mathcal{V}_\mu f$ corresponds to exactly one emitter distribution f .
- ③ **NUMERICAL ALGORITHM:** In Section 4 we derive a numerical algorithm for solving (2.10). Together with the FFT algorithm, this gives an efficient Fourier discrete reconstruction algorithm for reconstructing f from $\mathcal{V}_\mu f$. The proposed algorithm requires only $\mathcal{O}(N^2)$ floating point operations for reconstructing f at N discretization points.

- ④ **NUMERICAL STUDIES:** In Section 5 we present detailed numerical simulation studies and demonstrate that our algorithm yields accurate and fast reconstructions for data with and without Poisson noise. For reconstructing f at 40 000 discretization points, our algorithm only requires about 1/40 seconds on a standard PC. We further demonstrate that our method is stable with respect to the selection of the parameters involved.

To the best of our knowledge, these are the first analytic results for Compton camera image reconstruction accounting for non-vanishing attenuation.

For other Radon transforms, similar approaches have been previously and successfully applied in [2–4, 10, 17, 28, 30, 42]. However, in all these works the arising integral equations satisfy standard conditions needed in order to apply standard well-posedness results for generalized Abel equations. For (2.10), one main assumption required for such results is violated, since the kernels turn out to have zeros on the diagonal. Nevertheless, by using a recent result of [32] we are able to establish solution uniqueness of the attenuated V-line transform.

2 Fourier series decomposition

Throughout the following, $\mu \in \mathbb{R}$ denotes a fixed attenuation value. Our inversion approach uses the Fourier series with respect to the angular variables,

$$f(r\Phi(\varphi)) = \sum_{n \in \mathbb{Z}} f_n(r) e^{in\varphi}, \quad (2.1)$$

$$(\mathcal{V}_\mu f)(\varphi, \psi) = \sum_{n \in \mathbb{Z}} g_n(\psi) e^{in\varphi}, \quad (2.2)$$

where the Fourier coefficients of the emitter distribution and the corresponding attenuated V-line data are defined by

$$f_n(r) := \frac{1}{2\pi} \int_0^{2\pi} f(r\Phi(\varphi)) e^{-in\varphi} d\varphi, \quad (2.3)$$

$$g_n(\psi) := \frac{1}{2\pi} \int_0^{2\pi} (\mathcal{V}_\mu f)(\varphi, \psi) e^{-in\varphi} d\varphi. \quad (2.4)$$

Our strategy for inverting \mathcal{V}_μ is to recover each f_n from g_n . For that purpose we derive a one-dimensional integral equation for f_n in terms of g_n , which will subsequently be solved theoretically and numerically.

We will make use of the exponential Radon transform $\mathcal{T}_\mu f: [0, 2\pi) \times \mathbb{R} \rightarrow \mathbb{R}$ defined by

$$(\mathcal{T}_\mu f)(\alpha, s) := \int_{\mathbb{R}} f(s\Phi(\alpha) + t\Phi(\alpha)^\perp) e^{\mu t} dt. \quad (2.5)$$

The exponential Radon transform integrates the function f over the line $\{x \in \mathbb{R}^2 \mid \Phi(\alpha) \cdot x = s\}$ including the weight $e^{\mu t}$. It appears in image reconstruction in SPECT with Anger cameras. Its inversion has been addressed by many authors (see, for example, [9, 19, 21, 30, 39, 41]).

2.1 Auxiliary results

We start our analysis by writing $\mathcal{V}_\mu f$ as the sum of two exponential Radon transforms.

Lemma 2.1. *Suppose $f \in C_c^\infty(D_R)$. Then*

$$(\mathcal{V}_\mu f)(\varphi, \psi) = e^{-R\mu \cos(\psi)} \sum_{\sigma=\pm 1} (\mathcal{T}_{-\mu} f)(\pi/2 + \varphi - \sigma\psi, \sigma R \sin(\psi)). \quad (2.6)$$

Proof. With $\alpha := \frac{\pi}{2} + \varphi - \sigma\psi$ we have $\Phi(\varphi - \sigma\psi) = -\Phi(\alpha)^\perp$. A change of variables yields

$$\begin{aligned} & \int_0^\infty f(R\Phi(\varphi) - r\Phi(\varphi - \sigma\psi)) e^{-\mu r} dr \\ &= \int_{-R\cos(\psi)}^\infty f(\sigma R \sin(\psi)\Phi(\alpha) + t\Phi(\alpha)^\perp) e^{-\mu(R\cos(\psi)+t)} dt \\ &= e^{-\mu R \cos(\psi)} \int_{\mathbb{R}} f(\sigma R \sin(\psi)\Phi(\alpha) + t\Phi(\alpha)^\perp) e^{-t\mu} dt \\ &= e^{-\mu R \cos(\psi)} (\mathcal{T}_{-\mu} f)(\pi/2 + \varphi - \sigma\psi, \sigma R \sin(\psi)). \end{aligned}$$

Together with the definition of $\mathcal{V}_\mu f$, this gives (2.6). \square

Lemma 2.2. *Let $f \in C_c^\infty(D_R)$ and denote by $(\mathcal{T}_{-\mu} f)_n(s) := \frac{1}{2\pi} \int_0^{2\pi} (\mathcal{T}_{-\mu} f)(\alpha, s) e^{-in\alpha} d\alpha$. Then, for $(n, s) \in \mathbb{Z} \times \mathbb{R}$,*

$$(\mathcal{T}_{-\mu} f)_n(s) = \sum_{\sigma=\pm 1} \int_{|s|}^R f_n(r) e^{\sigma\mu\sqrt{r^2-s^2}} e^{-in\sigma \arccos(s/r)} \frac{r}{\sqrt{r^2-s^2}} dr. \quad (2.7)$$

Proof. Using the definitions of the Fourier coefficients, the exponential Radon transform and the one-dimensional δ -distribution, we obtain

$$\begin{aligned} & 2\pi(\mathcal{T}_{-\mu} f)_n(s) \\ &= \int_0^{2\pi} \int_{\mathbb{R}} f(s\Phi(\alpha) + t\Phi(\alpha)^\perp) e^{-\mu t} e^{-in\alpha} dt d\alpha \\ &= \int_0^{2\pi} \int_{\mathbb{R}^2} f(x) \delta(x \cdot \Phi(\alpha) - s) e^{-\mu x \cdot \Phi(\alpha)^\perp} e^{-in\alpha} dx d\alpha \\ &= \int_0^{2\pi} \int_0^{2\pi} \int_0^\infty f(r\Phi(\omega)) \delta(r \cos(\omega - \alpha) - s) \\ &\quad \times e^{-\mu r \sin(\omega - \alpha)} e^{-in\alpha} r dr d\omega d\alpha \\ &= \int_0^{2\pi} \int_0^{2\pi} \int_0^\infty f(r\Phi(\omega)) \delta(r \cos(u) - s) \\ &\quad \times e^{-\mu r \sin(u)} e^{-in\omega} e^{inu} r dr d\omega du \\ &= 2\pi \int_0^{2\pi} \int_0^\infty f_n(r) \delta(r \cos(u) - s) e^{-\mu r \sin(u)} e^{inu} r dr du. \end{aligned}$$

Recall $\delta(g(u)) = \sum_i \frac{\delta(u_i)}{|g'(u_i)|}$, where the sum is taken over all simple zeros of g . The zeros of $g(u) = r \cos(u) - s$ are given by $u_\pm = \pm \arccos(s/r)$. They satisfy $|g'(u_i)| = r |\sin(\arccos(s/r))| = \sqrt{r^2 - s^2}$, which yields (2.7). \square

2.2 Relation between the Fourier coefficients

In this section we derive two different relations between f_n and g_n . The first one (Thm. 2.3) is well suited for the numerical implementation, see Section 4. The second one (Lem. 2.4) will be used for uniqueness of reconstruction.

Theorem 2.3 (Generalized Abel equation for f_n). *Suppose $f \in C_c^\infty(D_R)$, and let f_n and g_n for $n \in \mathbb{Z}$ denote the Fourier coefficients of f and $\mathcal{V}_\mu f$. Then,*

$$\forall \psi \in (0, \pi/2) : \quad g_n(\psi) = 2e^{-\mu R \cos(\psi)} \int_{R \sin(\psi)}^R f_n(r) \frac{r K_n(R \sin(\psi), r)}{\sqrt{r^2 - R^2 \sin(\psi)^2}} dr, \quad (2.8)$$

with the kernel function

$$K_n(s, r) := \sum_{\sigma=\pm 1} \sigma^n e^{\sigma \mu \sqrt{r^2 - s^2}} \cos\left(n\left(\arcsin\left(\frac{s}{r}\right) - \sigma \arccos\left(\frac{s}{R}\right)\right)\right). \quad (2.9)$$

Proof. By Lem. 2.1 we have

$$\begin{aligned} & e^{\mu R \cos(\psi)} g_n(\psi) \\ &= \sum_{\sigma=\pm 1} e^{in(\pi/2 - \sigma\psi)} (\mathcal{T}_{-\mu} f)_n(\sigma R \sin(\psi)) \\ &= i^n \sum_{\sigma=\pm 1} e^{-in\sigma\psi} (\mathcal{T}_{-\mu} f)_n(\sigma R \sin(\psi)). \end{aligned}$$

Setting $s := R \sin(\psi)$ and using Lemma 2.2, we obtain

$$\begin{aligned} & (-i)^n e^{\mu R \cos(\psi)} g_n(\psi) \\ &= \sum_{\sigma_1, \sigma_2=\pm 1} \int_s^R \left[\frac{r f_n(r)}{\sqrt{r^2 - s^2}} e^{-in\sigma_1\psi} \right. \\ & \quad \left. \times e^{\sigma_2 \mu \sqrt{r^2 - s^2}} e^{-in\sigma_2 \arccos(\sigma_1 s/r)} \right] dr \\ &= \sum_{\sigma_1, \sigma_2=\pm 1} \int_s^R \left[\frac{r f_n(r)}{\sqrt{r^2 - s^2}} e^{-in\sigma_1\psi} \sigma_1^n \right. \\ & \quad \left. \times e^{\sigma_2 \mu \sqrt{r^2 - s^2}} e^{-\sigma_1 \sigma_2 in \arccos(s/r)} \right] dr \\ &= (-i)^n \sum_{\sigma_1, \sigma_2=\pm 1} \int_s^R \left[\frac{r f_n(r)}{\sqrt{r^2 - s^2}} e^{-in\sigma_1\psi} \right. \\ & \quad \left. \times \sigma_2^n e^{\sigma_2 \mu \sqrt{r^2 - s^2}} e^{\sigma_1 \sigma_2 in \arcsin(s/r)} \right] dr \\ &= 2(-i)^n \sum_{\sigma_2=\pm 1} \int_s^R \left[\frac{r f_n(r)}{\sqrt{r^2 - s^2}} \sigma_2^n e^{\mu \sigma_2 \sqrt{r^2 - s^2}} \right. \\ & \quad \left. \times \cos(n\psi - \sigma_2 n \arcsin(\frac{s}{r})) \right] dr. \end{aligned}$$

Here the second and third equalities follow from the identities $\arccos(-x) = \pi - \arccos(x)$, $\arccos(x) = \pi/2 - \arcsin(x)$. The last equality shows (2.8), (2.9). \square

For the following alternative relation between f_n and g_n we make use of the Chebyshev polynomials of the first kind,

$$T_k(z) := \cos(k \arccos(z)) \quad \text{for } |z| \leq 1.$$

We then have the following result.

Lemma 2.4. *Let $f \in C_0^\infty(D_R)$. For $n \in \mathbb{Z}$, let f_n, g_n denote the Fourier coefficients of f , $\mathcal{V}_\mu f$, and write*

$$\begin{aligned} (a) \quad \hat{g}_n(t) &:= \frac{1}{2} e^{\mu R \sqrt{t}} g_n(\arccos(\sqrt{t})); \\ (b) \quad \hat{f}_n(\rho) &:= R f_n(R \sqrt{1-\rho}); \\ (c) \quad \hat{K}_n(t, \rho) &:= \frac{1}{2} \sum_{\sigma=\pm 1} \sigma^n e^{\sigma \mu R \sqrt{t-\rho}} T_n\left(\frac{\sqrt{t}\sqrt{t-\rho} + \sigma(1-t)}{\sqrt{1-\rho}}\right). \end{aligned}$$

Then \hat{f}_n and \hat{g}_n are related via:

$$\forall t \in [0, 1]: \quad \hat{g}_n(t) = \int_0^t \hat{f}_n(\rho) \frac{\hat{K}_n(t, \rho)}{\sqrt{t-\rho}} d\rho. \quad (2.10)$$

Proof. By using the Chebyshev polynomials and using the trigonometric sum and difference identities we obtain

$$\begin{aligned} K_n(s, r) &= \sum_{\sigma=\pm 1} \sigma^n e^{\sigma \mu \sqrt{r^2-s^2}} T_n\left(\cos(\arcsin(\frac{s}{r}) - \sigma \arcsin(\frac{s}{R}))\right) \\ &= \sum_{\sigma=\pm 1} \sigma^n e^{\sigma \mu \sqrt{r^2-s^2}} T_n\left(\cos(\arcsin(\frac{s}{r})) \cos(\arcsin(\frac{s}{R}))\right. \\ &\quad \left.+ \sigma \sin(\arcsin(\frac{s}{r})) \sin(\arcsin(\frac{s}{R}))\right) \\ &= \sum_{\sigma=\pm 1} \sigma^n e^{\sigma \mu \sqrt{r^2-s^2}} T_n\left(\sqrt{1-\frac{s^2}{r^2}} \sqrt{1-\frac{s^2}{R^2}} + \sigma \frac{s}{r} \frac{s}{R}\right) \\ &= \sum_{\sigma=\pm 1} \sigma^n e^{\sigma \mu \sqrt{r^2-s^2}} T_n\left(\frac{\sqrt{r^2-s^2} \sqrt{R^2-s^2} + \sigma s^2}{rR}\right). \end{aligned}$$

Inserting the latter expression in (2.8), making the substitution $r^2 \leftarrow R^2 - R^2 \rho$ and using (a) yields

$$\begin{aligned} \hat{g}_n(t) &= \frac{1}{2} e^{\mu R \sqrt{t}} g_n(\arccos(\sqrt{t})) \\ &= \int_{R\sqrt{1-t}}^R \sum_{\sigma=\pm 1} \sigma^n \frac{e^{\sigma \mu \sqrt{r^2-R^2+R^2 t}}}{\sqrt{r^2-R^2+R^2 t}} \\ &\quad \times T_n\left(\frac{\sqrt{r^2-R^2+R^2 t} \sqrt{R^2 t} + \sigma R^2(1-t)}{rR}\right) f_n(r) r dr \end{aligned}$$

$$\begin{aligned}
&= \frac{1}{2}R \int_0^t f_n(R\sqrt{1-\rho}) \sum_{\sigma=\pm 1} \sigma^n e^{\sigma R\mu\sqrt{t-\rho}} \\
&\quad \times T_n\left(\frac{\sqrt{t-\rho}\sqrt{t} + \sigma(1-t)}{\sqrt{1-\rho}}\right) \frac{d\rho}{\sqrt{t-\rho}}.
\end{aligned}$$

With the definitions (b), (c) this gives (2.10). \square

3 Uniqueness of reconstruction

The integral equation (2.10) is of generalized Abel type. On the diagonal, the kernel \hat{K}_n takes the form

$$k_n(t) := \hat{K}_n(t, t) = T_n(\sqrt{1-t}). \quad (3.1)$$

Since the Chebyshev polynomials have zeros in $[0, 1]$, the same holds for the function $t \mapsto k_n(t)$. Consequently, standard theorems on well-posedness do not apply to (2.10), because such results require a non-vanishing diagonal.

3.1 General uniqueness result

In order to show solution uniqueness of (2.10), we use the following result that has recently been obtained in [32].

Lemma 3.1 (Uniqueness of generalized Abel equations with zeros on the diagonal, [32]). *Let the kernel $\hat{K}: \Delta \rightarrow \mathbb{R}$, with $\Delta := \{(t, \rho) \in [0, 1]^2 \mid 0 \leq \rho \leq t \leq 1\}$, satisfy the following:*

$$(K1) \quad \hat{K} \in C^3(\Delta).$$

$$(K2) \quad \text{The set of zeros } N(\hat{K}) := \{t \in [0, 1] \mid \hat{K}(t, t) = 0\} \text{ is finite and consists of simple zeros of } \hat{K}(t, t).$$

$$(K3) \quad \text{For every } t \in N(\hat{K}), (\beta_1, \beta_2) := \nabla \hat{K}(t, t) \text{ satisfies}$$

$$1 + \frac{1}{2} \frac{\beta_1}{\beta_1 + \beta_2} > 0. \quad (3.2)$$

Then, for any $\hat{g} \in C([0, 1])$, the generalized Abel equation

$$\forall t \in [0, 1]: \quad \hat{g}(t) = \int_0^t \frac{\hat{K}(t, \rho)}{\sqrt{t-\rho}} \hat{f}(\rho) d\rho \quad (3.3)$$

has at most one solution $f \in C([0, 1])$.

Proof. See [32, Thm. 3.4]. \square

3.2 Uniqueness of the attenuated V-line transform

We now apply Theorem 3.1 to show uniqueness of a solution of equation (2.10).

Theorem 3.2 (Uniqueness of recovering f_n). *Suppose $\mu R \leq 3/2$. For any $f \in C_0^\infty(D_R)$ and $n \in \mathbb{Z}$, the Fourier coefficient f_n can be recovered as the unique solution of (2.8).*

Proof. Let $f \in C_0^\infty(D_R)$ vanish outside a ball of Radius $R^2 - R^2 a^2$ with $a < 1$. According to Lem. 2.4, it is sufficient to show that (2.10) has a unique solution. To show that this is the case, we apply Lem. 3.1 by verifying that \hat{K}_n satisfies (K1)-(K3). Clearly, \hat{K}_n is smooth for $t \neq \rho$. Further, \hat{K}_n can be written as power series only containing even powers of $\sqrt{st - \rho}$. Consequently, \hat{K}_n is also smooth on $\{(t, \rho) \in \Delta \mid t = \rho\}$, which shows (K1). Next, recall $k_n(t) := \hat{K}_n(t, t) = T_n(\sqrt{1-t})$. As T_n has a finite number of isolated and simple roots this implies (K2).

It remains to verify (K3). For that purpose, let $t_0 \in [a, 1)$ be a zero of k_n and set $(\beta_1, \beta_2) := \nabla K_n(t_0, t_0)$. Then

$$\beta_1 + \beta_2 = k'_n(t_0) = -\frac{1}{2\sqrt{1-t_0}} T'_n(\sqrt{1-t_0}). \quad (3.4)$$

Next we compute $\beta_1 = (\beta_1 + \beta_2) - \beta_2$. For small ϵ ,

$$\begin{aligned} & 2\hat{K}_n(t_0, t_0 - \epsilon) \\ &= \sum_{\sigma=\pm 1} \sigma^n e^{\sigma \mu R \sqrt{\epsilon}} T_n\left(\frac{\sqrt{t_0} \sqrt{\epsilon} + \sigma(1-t_0)}{\sqrt{1-t_0} + \epsilon}\right) \\ &= \sum_{\sigma=\pm 1} \sigma^n (1 + \sigma \mu R \sqrt{\epsilon}) \left(\frac{\sqrt{t_0} T'_n(\sigma \sqrt{1-t_0})}{\sqrt{1-t_0}} \sqrt{\epsilon} \right. \\ &\quad \left. + \left[\frac{t_0 T''_n(\sigma \sqrt{1-t_0})}{2(1-t_0)} - \frac{\sigma T'_n(\sigma \sqrt{1-t_0})}{2\sqrt{1-t_0}} \right] \epsilon \right) + \mathcal{O}(\epsilon^2) \\ &= \frac{1}{\sqrt{1-t_0}} \left((2\mu R \sqrt{t_0} - 1) T'_n(\sqrt{1-t_0}) \right. \\ &\quad \left. + \frac{t_0 T''_n(\sqrt{1-t_0})}{\sqrt{1-t_0}} \right) \epsilon + \mathcal{O}(\epsilon^2). \end{aligned}$$

Here for the last equality we used $T'_n(-x) = (-1)^{n+1} T'_n(x)$ and $T''_n(-x) = (-1)^n T''_n(x)$. Because T_n is a solution of the differential equation $(1-x^2) T''_n(x) - x T'_n(x) + n^2 T_n(x) = 0$ and t_0 is a zero of $t \mapsto T_n(\sqrt{1-t})$, it follows that $-\beta_2 = \frac{\mu R \sqrt{t_0}}{\sqrt{1-t_0}} T'_n(\sqrt{1-t_0})$. Together with (3.4) we obtain

$$\beta_1 = \frac{2\mu R \sqrt{t_0} - 1}{\sqrt{1-t_0}} T'_n(\sqrt{1-t_0}). \quad (3.5)$$

From (3.4) and (3.5) we finally conclude

$$1 + \frac{1}{2} \frac{\beta_1}{\beta_1 + \beta_2} = 1 - \frac{2\mu R \sqrt{t_0} - 1}{2} = \frac{3}{2} - \mu R \sqrt{t_0} > 0,$$

which is (K3). Consequently, Lem. 3.1 implies that \hat{f}_n is the unique solution of (2.4). \square

As a corollary of Thm. 3.2 we immediately obtain the following uniqueness result for the attenuated V-line transform.

Corollary 3.3 (Invertibility of \mathcal{V}_μ). *Suppose $\mu R \leq 3/2$. If $f_1, f_2 \in C_0^\infty(D_R)$ satisfy $\mathcal{V}_\mu f_1 = \mathcal{V}_\mu f_2$, then $f_1 = f_2$.*

Proof. Let $f \in C_0^\infty(D_R)$ satisfy $(\mathcal{V}_\mu f)_n = 0$ for all $n \in \mathbb{Z}$. Thm. 3.2 shows that (2.8) has the unique solution $f_n = 0$, which implies $f = 0$. The linearity of \mathcal{V}_μ gives the claim. \square

For the case of vanishing attenuation, in [26] we derived an explicit solution formula for (2.8). We have not been able to derive a similar result $\mu \neq 0$; currently we don't know whether such a solution formula exists. In the following section we show that (2.8) can be efficiently solved numerically.

4 Numerical reconstruction algorithm

In this section we numerically implement the Fourier series approach. Suppose we have given discrete data

$$\mathbf{g}[p, q] \simeq \mathcal{V}_\mu f(\varphi_p, \arcsin(s_q/R)) \quad \text{for } (p, q) \in \{0, \dots, P-1\} \times \{0, \dots, Q\}. \quad (4.1)$$

Here $\varphi_p := 2\pi p/P$ and $s_q := qR/Q$ correspond to discrete vertex positions and half opening angles. The goal is to estimate the values $f(x_i)$ of the emission distribution at grid points $x_i = (i_1, i_2)R/M$ for $i = (i_1, i_2) \in \{-M, \dots, M\}^2$.

4.1 Basic reconstruction strategy

Thm. 2.3 shows that f can be recovered from $\mathcal{V}_\mu f$ by implementing the following steps:

(S1) Evaluate $g_n(\psi) := \int_0^{2\pi} (\mathcal{V}_\mu f)(\varphi, \psi) e^{-in\varphi} d\varphi$.

(S2) Estimate f_n by solving (2.8).

(S3) Evaluate $f(r\Phi(\varphi)) = \sum_{n \in \mathbb{Z}} f_n(r) e^{in\varphi}$.

(S4) Resample f to Cartesian coordinates.

As described in the following, in our numerical implementation we discretize any of these steps. For (S1) and (S3), we use the standard FFT algorithm. For (S1), the FFT algorithm outputs approximations to g_n , which are used as inputs for (S2). After implementing (S3), we have an approximation of f given on a polar grid. For resampling these values to a Cartesian grid, we use bilinear interpolation in the polar coordinate space.

The main issue in the reconstruction procedure consists in solving the integral equation (2.8). For that purpose we use the product integration method with the mid-point rule [23, 29, 40], that is presented in the following subsection.

4.2 The product integration method for solving (2.8)

Evaluating (2.8) at the discretization points s_q yields

$$\begin{aligned}\tilde{g}_n(s_q) &:= \frac{e^{\mu\sqrt{R^2-s_q^2}}}{2} g_n\left(\arcsin\left(\frac{s_q}{R}\right)\right) \\ &= \sum_{j=q}^{Q-1} \int_{s_j}^{s_{j+1}} f_n(r) \frac{r K_n(s_q, r)}{\sqrt{r^2 - s_q^2}} dr.\end{aligned}$$

Approximating $K_n(s_q, r) \simeq K_n(s_q, r_j)$ on $r \in [s_j, s_{j+1}]$ where $r_j := (j + 1/2) R/Q$, we obtain

$$\begin{aligned}\tilde{g}_n(s_q) &\simeq \sum_{j=q}^{Q-1} w_{q,j} K_n(s_q, r_j) f_n(r_j), \\ w_{q,j} &:= \int_{s_j}^{s_{j+1}} \frac{r}{\sqrt{r^2 - s_q^2}} dr = \sqrt{s_{j+1}^2 - s_q^2} - \sqrt{s_j^2 - s_q^2}.\end{aligned}$$

Set $w_{q,j} = 0$ for $j \geq q$ and define

- ❖ discrete kernels $\mathbf{K}_n = (w_{q,j} K_n(s_q, r_j))_{q,j=0,\dots,Q-1}$;
- ❖ discrete data $\tilde{\mathbf{g}}_n = (\tilde{g}_n(s_0), \dots, \tilde{g}_n(s_{Q-1}))^\top$;
- ❖ discrete unknowns $\mathbf{f}_n = (f_n[0], \dots, f_n[Q-1])^\top$.

The product integration method then consists in solving the following system of linear equations:

$$\text{Find } \mathbf{f}_n \in \mathbb{R}^Q \text{ such that } \tilde{\mathbf{g}}_n = \mathbf{K}_n \mathbf{f}_n. \quad (4.2)$$

The matrix \mathbf{K}_n is triangular. If \mathbf{K}_n is non-singular, then (4.2) can efficiently be solved by forward substitution.

4.3 Tikhonov regularization

Because the kernel function K_n has zeros in the diagonal, the matrix \mathbf{K}_n has diagonal entries being close to zero. As a consequence, solving (4.2) is numerically unstable. In order to obtain stable solutions, regularization methods have to be applied. We apply Tikhonov regularization [12, 15, 18, 31, 37] for that purpose, where regularized solutions \mathbf{f}_n^λ are defined as solutions of the regularized normal equation

$$(\mathbf{K}_n^\top \mathbf{K}_n + \lambda_n \mathbf{I}_Q) \mathbf{f}_n^\lambda = \mathbf{K}_n^\top \tilde{\mathbf{g}}_n. \quad (4.3)$$

Here \mathbf{I}_Q is the $Q \times Q$ identity matrix and $\lambda = (\lambda_n)_n$ a vector of non-negative regularization parameters.

For a non-vanishing kernel diagonal, the product integration method (4.2) is known to be convergent of order 3/2; see [40, Theorem 3.5]. Due to the zeros of the kernels, such results cannot be applied to the attenuated V-line transform. We are not aware of any results in that direction. The numerical results indicate that for suitable selection of the regularization parameter, a convergence analysis should be possible.

4.4 Summary of reconstruction algorithm

In summary, we obtain the following reconstruction algorithm for inverting the attenuated V-line transform.

Algorithm 4.1 (Numerical inversion of the attenuated V-line transform).

Input: Data $\mathbf{g} = (\mathbf{g}[p, q])_{p,q} \in \mathbb{R}^{P \times (Q+1)}$; see (4.1).

Output: $\mathbf{f}^\lambda \simeq (f(x_i))_i \in \mathbb{R}^{(2M+1) \times (2M+1)}$.

(N1) Apply the FFT: $(\mathbf{g}_n)_n := \text{FFT}(\mathbf{g})$.

(N2) For any $n = -P/2, \dots, P/2 - 1$ do:

- ❖ Set $\tilde{g}_n(s_q) := \frac{1}{2} \exp(\mu \sqrt{R^2 - s_q^2}) g_n(\arcsin(\frac{s_q}{R}))$;
- ❖ Choose regularization parameters $\lambda_n > 0$;
- ❖ Compute \mathbf{f}_n^λ by solving (4.3).

(N3) Apply the inverse FFT: $\mathbf{f}_{\text{POL}}^\lambda := \text{IFFT}((\mathbf{f}_n^\lambda)_n)$.

(N4) Resample $\mathbf{f}_{\text{POL}}^\lambda$ to a Cartesian grid.

Steps (N1) and (N3) in Alg. 4.1 consist of Q one-dimensional FFTs and therefore require $\mathcal{O}(QP \log P)$ floating point operations (FLOPS). Using bilinear interpolation (N4) requires $\mathcal{O}(M^2)$ FLOPS. The most time consuming part is (N2) which consists of solving the P linear equations (4.3), each with Q unknowns. Using the Cholesky decomposition these equations are solved with approximately $Q^3/6$ FLOPS. Supposing $P, Q, M = \mathcal{O}(N^{1/2})$, where N is the total number of unknowns, the numerical effort of Alg. 4.1 therefore is $\mathcal{O}(N^2)$ with a small leading constant. On a standard PC, our algorithm requires about 1/40 seconds for recovering about $N = 40\,000$ unknowns.

5 Numerical results

For the following numerical results we use the true emission distribution (phantom) \mathbf{f}^\star shown in Fig. 4.1(a). It is contained in the disc of radius $R = 8$ cm and represented by discrete values on an $(2M+1) \times (2M+1)$ grid with $M := 100$. Attenuated V-line data are simulated for $P = 100$ vertex positions indicated by white dots in Fig. 4.1(a). At every vertex position we evaluate the attenuated V-line transform for $Q+1$ half opening angles with $Q := 100$. The attenuation coefficient is taken as $\mu = 0.15/\text{cm}$.

5.1 Data computation

For numerically computing the attenuated V-line transform, each of the two branches of the V-line with vertex $R\Phi(\varphi_p)$ and half opening angle ψ_q is sampled at $2M+1$ equidistant

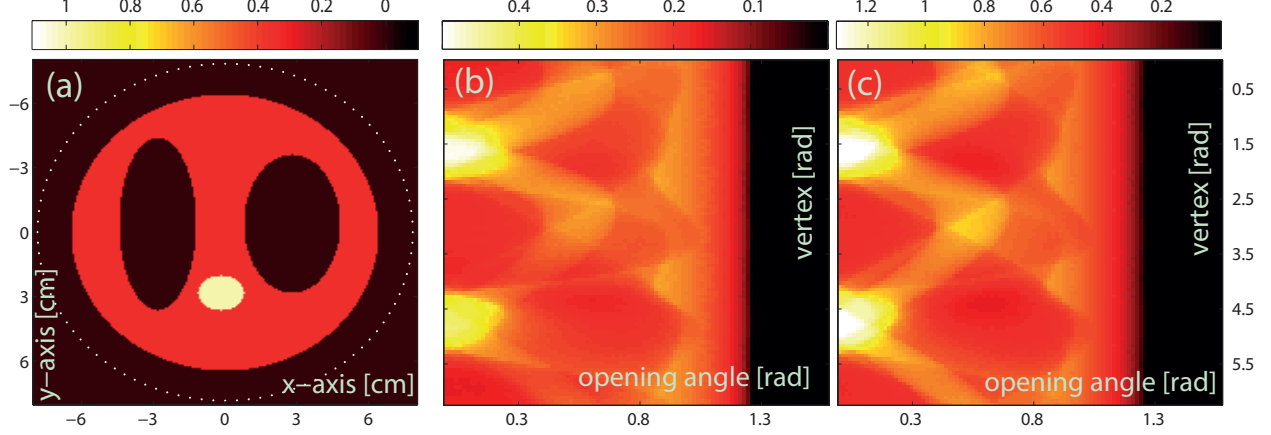


Figure 4.1: PHANTOM AND DATA. (a) Emission distribution (phantom) evaluated at a uniform $(2M + 1) \times (2M + 1)$ grid used for simulation studies. (b) Attenuated V-line transform with $\mu = 0.15$ /cm (c) Un-attenuated V-line transform.

discretization points in the interval $[0, 2R]$. The approximate function values $f_{\text{BL}}(R\Phi(\varphi_p) - j\frac{2R}{M}\Phi(\varphi_p - \sigma\psi_q))$ are computed by bilinear interpolation. Given these approximate function values, we find

$$g[p, q] := \frac{2R}{M} \sum_{\sigma=\pm 1} \sum_{j=0}^M f_{\text{BL}}(R\Phi(\varphi_p) - \frac{2R}{M}j\Phi(\varphi_p - \sigma\psi_q)) e^{-2\mu jR/M} \quad (5.1)$$

as an approximation to $\mathcal{V}_\mu f(\varphi_p, \psi_q)$.

The numerically computed attenuated V-line data corresponding to the phantom of Fig. 4.1(a) are shown in Fig. 4.1(b). For comparison purpose Fig. 4.1(c) shows the V-line transform of the same phantom computed with attenuation value zero. One clearly notes two effects of attenuation: First, compared to unattenuated data, the overall intensity of the data is reduced. Second, and more importantly, the attenuation effects change non-uniformly over the data domain, which makes attenuation correction a non-trivial issue.

5.2 Reconstruction results for simulated data

Next we present results of Alg. 4.1 applied to the data shown in Fig. 4.1. The first issue that has to be addressed is the selection of the regularization parameter. For that purpose, Fig. 5.1(a) displays the condition numbers $\kappa(\mathbf{K}_n) := \|\mathbf{K}_n\| \|\mathbf{K}_n^{-1}\|$, which are a measure for the instability of solving (4.2). Except for $n = 0$, the condition numbers are large. Hence we stabilize any of the equations (4.2) except the one for $n = 0$. To get more inside in the instability of (4.2), Fig. 5.1(c) shows the singular values of \mathbf{K}_n . For any of the matrices with $n \neq 0$, one observes a quite similar behavior. Therefore we use a constant positive regularization parameter for $n \neq 0$. Such a choice turns out to perform well in our numerical studies. Selecting the scalar regularization parameter still is a non-trivial issue. In the current studies we have chosen it empirically by testing different values. Data driven strategies such

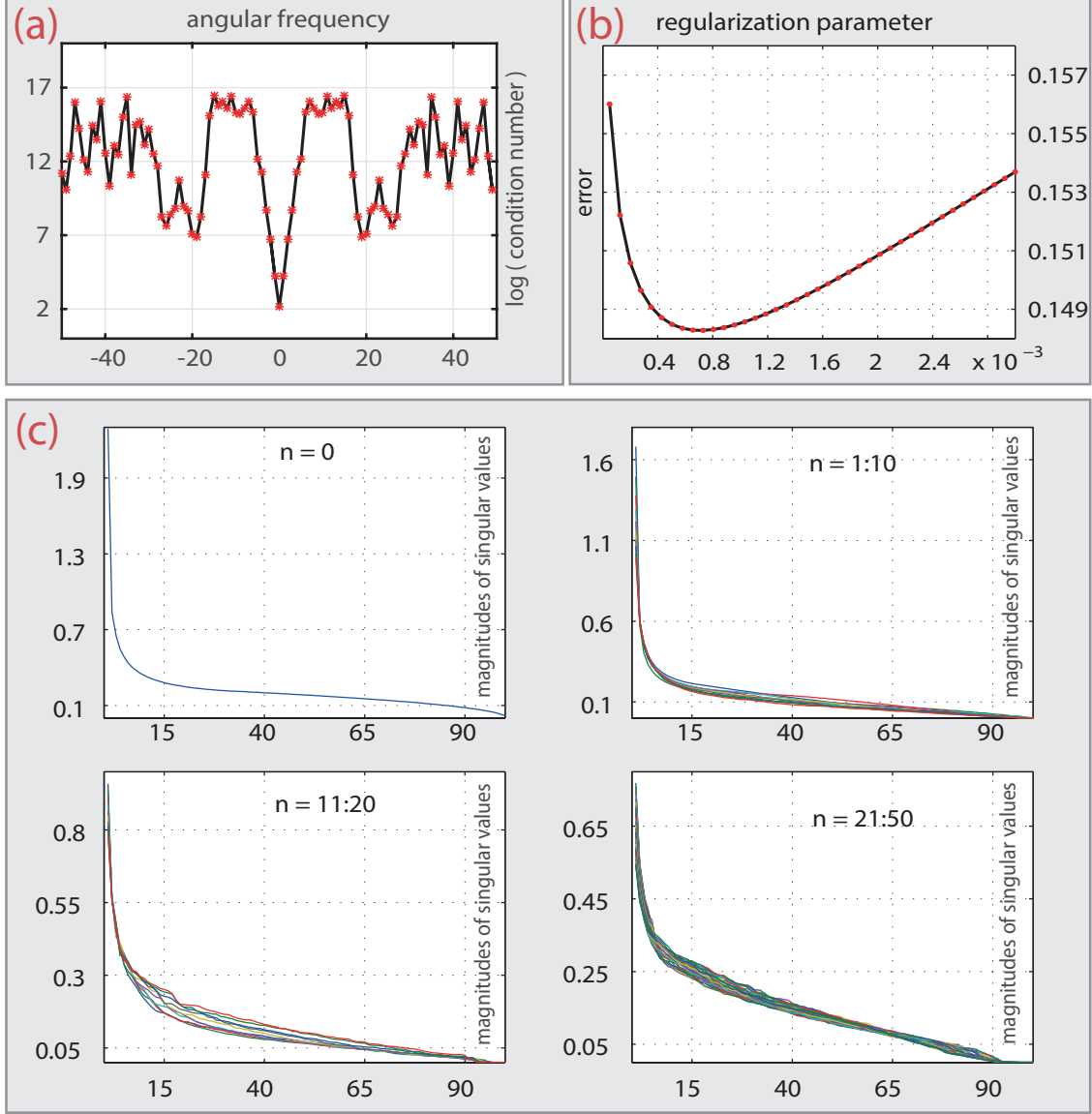


Figure 5.1: INVESTIGATION OF STABILITY. (a) Condition numbers of \mathbf{K}_n . (b) Relative ℓ^2 -reconstruction error as a function of the regularization parameter. (c) Singular values of \mathbf{K}_n for $n = 0$ (top left), $n = 1, \dots, 10$ (top right), $n = 11, \dots, 20$ (bottom left), and $n = 21, \dots, 50$ (bottom right).

as the discrepancy principle or the L-curve method [12, 18] will be investigated in future studies.

For Fig. 5.1(b) we compute the relative ℓ^2 -reconstruction errors $\|\mathbf{f}^* - \mathbf{f}^\lambda\|_2 / \|\mathbf{f}^*\|_2$ for different values of the regularization parameter λ . One observes the typical semi-convergence behavior expected for ill-posed problems: Starting with a large regularization parameter λ , the error first decreases with decreasing λ up to an optimal λ^* . A further decrease of λ increases the error due to over-fitting of the data. In the present case, the optimal regularization parameter turns out to be $\lambda^* \simeq 0.0008$. The corresponding reconstruction

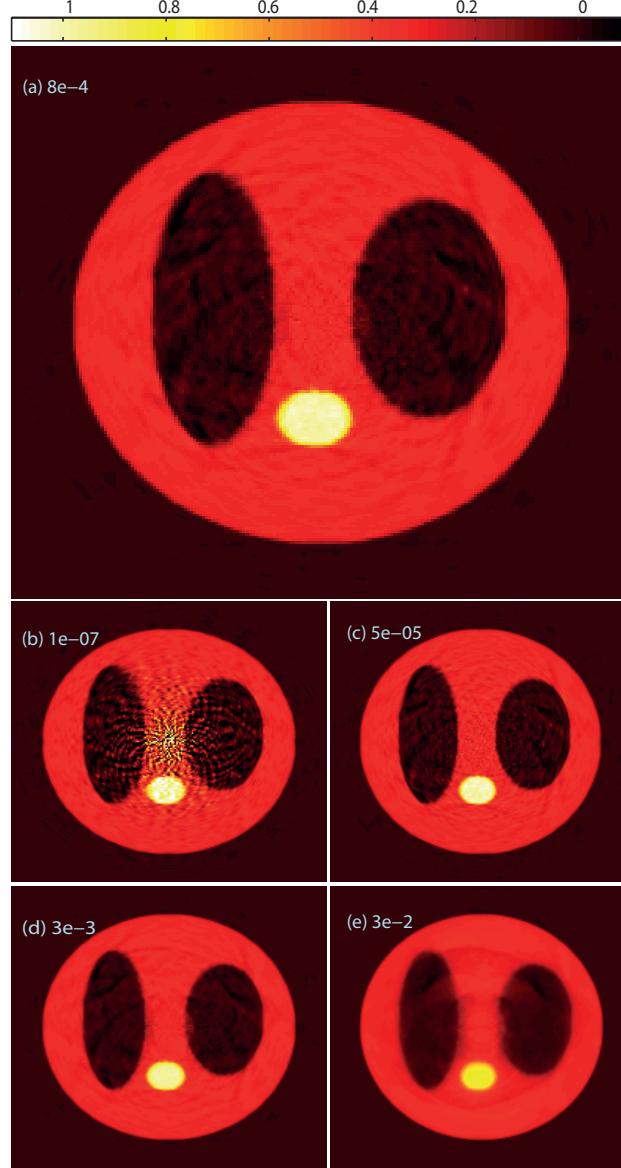


Figure 5.2: RECONSTRUCTIONS FROM SIMULATED DATA. The regularization parameter has been chosen close to optimal value in (a), very small in (b), small in (c), large in (d) and very large in (e).

result is shown in Fig. 5.2(a).

Fig. 5.2(c) and Fig. 5.2(d) show reconstructions for not optimally selected regularization parameters. The reconstruction results are still good which demonstrates the stability of our algorithm with respect to the choice of the regularization parameter. In particular, a wide range of parameters can be used to obtain accurate reconstructions. However, λ cannot be chosen arbitrary far away from the optimal value: Fig. 5.2(b) corresponds to a small regularization parameter far away from the optimal value. High frequency error is evident. Fig. 5.2(e) shows results for a much too large regularization parameter resulting in a blurred

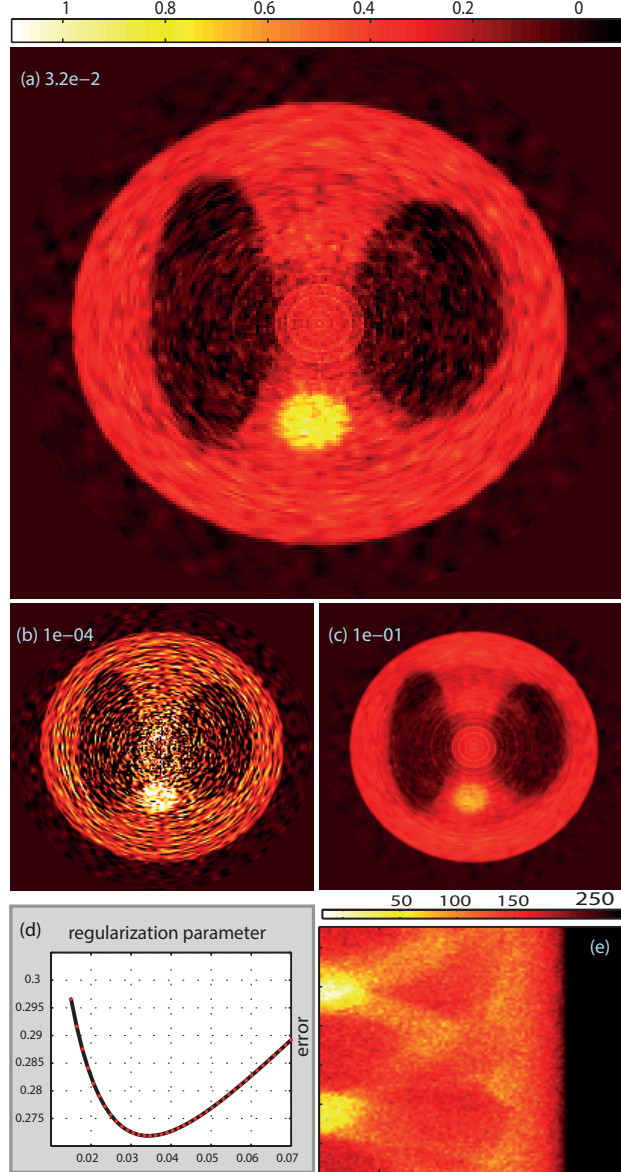


Figure 5.3: NOISY DATA SIMULATIONS. (a) Reconstruction using optimal λ . (b) Reconstruction results using too small λ . (c) Reconstruction results using too large λ . (d) Relative ℓ^2 reconstruction error for various λ (e) Photon limited noisy data.

reconstruction.

5.3 Reconstruction results for photon limited data

An extremely important feature of any image reconstruction algorithm is its ability to deal with noisy data. In order to investigate this issue, we performed simulations for limited number of photon counts. For the data shown in Fig. 5.3(e) we use a total number of 1 894 918 photon counts and a maximal number of 573 photon counts on a single V-line.

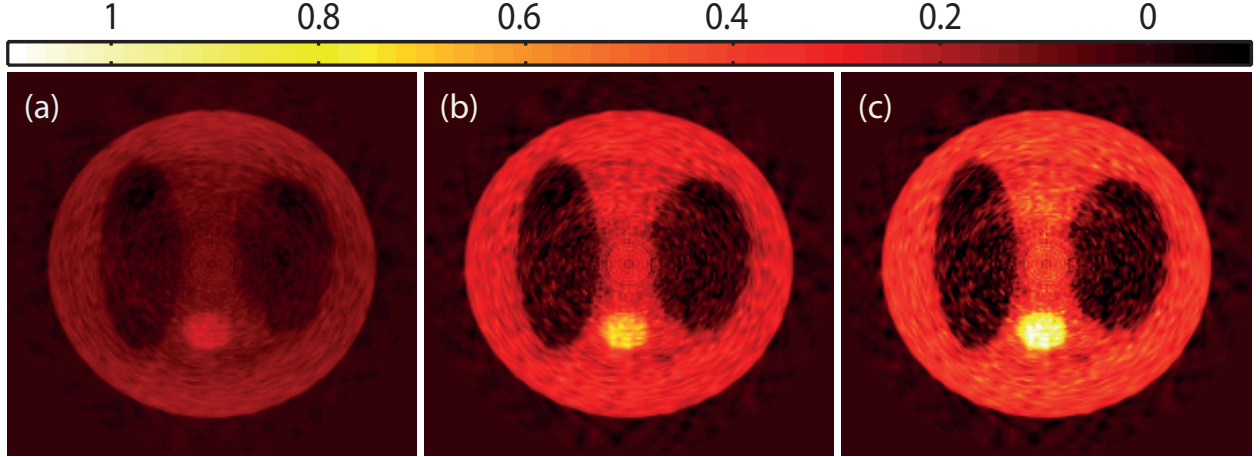


Figure 5.4: STABILITY WITH RESPECT TO CORRECT ATTENUATION VALUE. (a) Reconstruction from data shown in Fig. 5.3 using Alg. 4.1 with $\lambda = 0.03$ and assuming vanishing attenuation. (b) Same for under-estimated attenuation $\mu = 0.125$ /cm. (c) Same for over-estimated attenuation $\mu = 0.175$ /cm. The data is shown in Fig. 5.3 and has true attenuation value $\mu = 0.15$ /cm.

The reconstruction results for different regularization parameters are shown in Figs. 5.3(a)-(c): In Fig. 5.3(a), the regularization parameter is chosen close to the optimal value, while in Fig. 5.3(b) it is chosen much too small, and in Fig. 5.3(c) it is chosen much too large. The same qualitative behavior as for simulated data can be observed. However, as expected, the optimal regularization parameter is much larger and the reconstruction results worse than in the simulated data case. The dependence on the regularization parameter has been investigated by computing the relative ℓ^2 -error shown in Fig. 5.3(d).

In practical applications the attenuation value μ may not be known exactly. We therefore apply Alg. 4.1 with attenuation values that are different from the true attenuation. Results are shown in Fig. 5.4 where we used the same noisy data as above and a regularization parameter of $\lambda = 0.03$. One notices that the reconstruction results are quite stable with respect to the correct attenuation value. On the other hand, the poor reconstruction quality assuming vanishing attenuation shown in Fig. 5.4(a) clearly demonstrates that ignoring attenuation produces unacceptable results.

6 Conclusion

In this paper we established a Fourier series approach for inverting the attenuated V-line transform arising in SPECT with Compton cameras. We have been able to show invertibility of the attenuated V-line transform and to derive an efficient reconstruction algorithm.

It is an interesting line of future work to generalize our results in various directions. For example, similar inversion approaches may be derived for various geometries in two dimensions (attenuated V-line transforms) and three dimensions (attenuated conical Radon transform). Further interesting extensions consider the case of non-orthogonal axis and non-

constant attenuation. Finally, comparing our approach with iterative methods and testing on real data are important future aspects.

Acknowledgment

The work of S. Moon has been supported by the National Research Foundation of Korea grant funded by the Korea government (MSIP) (2015R1C1A1A01051674) and the TJ Park Science Fellowship of POSCO TJ Park Foundation. S. Moon thanks the University of Innsbruck for hospitality during his visit, when parts of this work have been carried out.

References

- [1] M. Allmaras, D. Darrow, Y. Hristova, G. Kanschat, and P. Kuchment. Detecting small low emission radiating sources. *Inverse Probl. Imaging*, 7(1):47–79, 2013.
- [2] G. Ambartsoumian, R. Gouia-Zarrad, and M. A. Lewis. Inversion of the circular Radon transform on an annulus. *Inverse Probl.*, 26(10):105015, 11, 2010.
- [3] G. Ambartsoumian and S. Moon. A series formula for inversion of the V-line Radon transform in a disc. *Comput. Math. Appl.*, 66(9):1567–1572, 2013.
- [4] G. Ambartsoumian and S. Roy. Numerical inversion of a broken ray transform arising in single scattering optical tomography. *IEEE Trans. Comput. Imaging*, 2(2):166–173, 2016.
- [5] H. O. Anger. Scintillation camera. *Rev. Sci. Instr.*, 29(1):27–33, 1958.
- [6] R. Basko, G. L. Zeng, and G. T. Gullberg. Analytical reconstruction formula for one-dimensional Compton camera. *IEEE Trans. Nucl. Sci.*, 44(3):1342–1346, 1997.
- [7] R. Basko, G. L. Zeng, and G. T. Gullberg. Application of spherical harmonics to image reconstruction for the Compton camera. *Phys. Med. Biol.*, 43(4):887, 1998.
- [8] R. Basko, G.L. Zeng, and G.T. Gullberg. Fully three dimensional image reconstruction from V-projections acquired by Compton camera with three vertex electronic collimation. In *Nuclear Science Symposium, 1997. IEEE*, volume 2, pages 1077–1081, 1997.
- [9] S. Bellini, M. Piacentini, C. Cafforio, and F. Rocca. Compensation of tissue absorption in emission tomography. *IEEE Trans. Acoust., Speech, Signal Processing*, 27(3):213–218, 1979.
- [10] A. M. Cormack. Representation of a function by its line integrals, with some radiological applications. *J. Appl. Phys.*, 34(9):2722–2727, 1963.
- [11] M. J. Cree and P. J. Bones. Towards direct reconstruction from a gamma camera based on Compton scattering. *IEEE Trans. Med. Imaging*, 13(2):398–407, 1994.

- [12] H. W. Engl, M. Hanke, and A. Neubauer. *Regularization of inverse problems*, volume 375 of *Mathematics and its Applications*. Kluwer Academic Publishers Group, Dordrecht, 1996.
- [13] D. B. Everett, J. S. Fleming, R. W. Todd, and J. M. Nightingale. Gamma-radiation imaging system based on the Compton effect. *Proc. IEEE*, 124(11):995–1000, 1977.
- [14] Rim Gouia-Zarrad and Gaik Ambartsoumian. Exact inversion of the conical Radon transform with a fixed opening angle. *Inverse Probl.*, 30(4):045007, 12, 2014.
- [15] C. W. Groetsch. *The Theory of Tikhonov Regularization for Fredholm Equations of the First Kind*. Pitman, Boston, 1984.
- [16] M. Haltmeier. Exact reconstruction formulas for a Radon transform over cones. *Inverse Probl.*, 30(3), 2014.
- [17] E. W. Hansen. Circular harmonic image reconstruction: experiments. *Appl. Opt.*, 20(13):2266–2274, 1981.
- [18] P. C. Hansen. *Rank-Deficient and Discrete Ill-Posed Problems*. SIAM Monographs on Mathematical Modeling and Computation. SIAM, Philadelphia, PA, 1998.
- [19] W. G. Hawkins, P. K. Lechner, and N.-C. Yang. The circular harmonic transform for spect reconstruction and boundary conditions on the fourier transform of the sinogram. *IEEE Trans. Med. Imag.*, 7(2):135–138, 1988.
- [20] M. Hirasawa and T. Tomitani. An analytical image reconstruction algorithm to compensate for scattering angle broadening in Compton cameras. *Phys. Med. Biol.*, 48(8):1009, 2003.
- [21] T. Inouye, K. Kose, and A. Hasegawa. Image reconstruction algorithm for single-photon-emission computed tomography with uniform attenuation. *Physics in Medicine and Biology*, 34(3):299–304, 1989.
- [22] C. Jung and S. Moon. Inversion formulas for cone transforms arising in application of Compton cameras. *Inverse Probl.*, 31(1):015006, 20, 2015.
- [23] P. Linz. *Analytical and numerical methods for Volterra equations*, volume 7 of *SIAM Studies in Applied Mathematics*. SIAM, Philadelphia, PA, 1985.
- [24] V. Maxim, M. Frandeg, and R. Prost. Analytical inversion of the Compton transform using the full set of available projections. *Inverse Probl.*, 25(9):095001, 21, 2009.
- [25] S. Moon. On the determination of a function from its conical Radon transform with a fixed central axis. *SIAM J. Math. Anal.*, 48(3):1833–1847, 2016.
- [26] S. Moon and M. Haltmeier. Analytic inversion of a conical Radon transform arising in application of Compton cameras on the cylinder. <http://arxiv.org/abs/1607.00867>, 2016.

- [27] M. Morvidone, M. K. Nguyen, T. T. Truong, and H. Zaidi. On the V-line Radon transform and its imaging applications. *Int. J. Biomed. Imaging*, 2010:208179, 6, 2010.
- [28] R. M. Perry. Reconstructing a function by circular harmonic analysis of line integrals. In *Image Processing for 2-D and 3-D Reconstruction from Projections: Theory and Practice in Medicine and the Physical Sciences*. Digest of technical papers, Stanford, California, 1975.
- [29] R. Plato. The regularizing properties of the composite trapezoidal method for weakly singular Volterra integral equations of the first kind. *Adv. Comput. Math.*, 36(2):331–351, 2012.
- [30] Alfred Puro. Cormack-type inversion of exponential Radon transform. *Inverse Problems*, 17(1):179, 2001.
- [31] O. Scherzer, M. Grasmair, H. Grossauer, M. Haltmeier, and F. Lenzen. *Variational methods in imaging*, volume 167 of *Applied Mathematical Sciences*. Springer, New York, 2009.
- [32] Daniela Schiefeneder and Markus Haltmeier. The Radon transform over cones with vertices on the sphere and orthogonal axes, 2016.
- [33] M. Singh. An electronically collimated gamma camera for single photon emission computed tomography. part I: Theoretical considerations and design criteria. *Med. Phys.*, 10(421):1983, 1983.
- [34] B. Smith. Reconstruction methods and completeness conditions for two Compton data models. *J. Opt. Soc. Am. A*, 22(3):445–459, 2005.
- [35] B. Smith. Line-reconstruction from Compton cameras: data sets and a camera design. *Opt. Eng.*, 50(5):053204, 2011.
- [36] F. Terzioglu. Some inversion formulas for the cone transform. *Inverse Probl.*, 31(11):115010, 21, 2015.
- [37] A. N. Tikhonov and V. Y. Arsenin. *Solutions of Ill-Posed Problems*. John Wiley & Sons, Washington, D.C., 1977.
- [38] R. W. Todd, J. M. Nightingale, and D. B. Everett. A proposed gamma camera. *Nature*, 251:132–134, 1974.
- [39] O. Tretiak and C. Metz. The exponential Radon transform. *SIAM J. Appl. Math.*, 39(2):341–354, 1980.
- [40] R. Weiss and R. S. Anderssen. A product integration method for a class of singular first kind Volterra equations. *Numer. Math.*, 18:442–456, 1971.

- [41] C. E. Yarman and B. Yazici. A new exact inversion method for exponential Radon transform using the harmonic analysis of the Euclidean motion group. *Inverse Probl. Imaging*, 1(3):457–479, 2007.
- [42] J. You, Z. Liang, and G. L. Zeng. A unified reconstruction framework for both parallel-beam and variable focal-length fan-beam collimators by a Cormack-type inversion of exponential Radon transform. *IEEE Trans. Med. Imag.*, 18(1):59–65, 1999.